Available online at www.sciencedirect.com
ScienceDirect
International Journal of Heat and Mass Transfer 51 (2008) 2847–2862
International Journal of HEAT and MASS TRANSFER
www.elsevier.com/locate/ijhmt

A coupled thermo-hydro-mechanical-damage model for concrete subjected to moderate temperatures

Benoît Bary [a,*], Guillaume Ranc [b], Sabine Durand [c], Olivier Carpentier [a]

[a] CEA Saclay, DEN/DPC/SCCME/LECBA, 91191 Gif/Yvette, France
[b] CEA VALRHO, DEN/DTEC/L2EC/LCEC, 30207 Bagnols sur Cèze, France
[c] CEA Saclay, DEN/DM2S/SEMT/LM2S, 91191 Gif/Yvette, France

Received 4 July 2007
Available online 7 November 2007

Abstract

This study focuses on the concrete behavior subjected to moderate temperatures, with a particular emphasis on the transient thermo-hydric stage. A simplified coupled thermo-hydro-mechanical model is developed with the assumption that the gaseous phase is composed uniquely of vapor. Estimations of the mechanical parameters, Biot coefficient and permeability as a function of damage and saturation degree are provided by applying effective-medium approximation schemes. The isotherm adsorption curves are supposed to depend upon both temperature and crack-induced porosity. The effects of damage and parameters linked to transfer (in particular the adsorption curves) on the concrete structure response in the transient phase of heating are then investigated and evaluated. To this aim, the model is applied to the simulation of concrete cylinders with height and diameter of 0.80 m subjected to heating rates of 0.1 and 10 °C/min up to 160 °C. The numerical results are analyzed, commented and compared with experimental ones in terms of water mass loss, temperatures and gas pressures evolutions. A numerical study indicates that some parameters have a greater influence on the results than others, and that certain coupling terms in the mass conservation equation of water may be neglected.

Keywords: Modeling; Thermo-hydro-mechanical coupling; Numerical simulations; Concrete; Damage; Water transfers

1. Introduction

The behavior of concrete is a topic of great concern in the context of radioactive waste management where these materials could be intensively used in the construction of interim storage structures. In such conditions, concrete is typically subjected to thermal and mechanical loadings inducing moisture transfers spanning over several centuries. Similar loading conditions may also be encountered in nuclear plant containments undergoing temporary accidental situations. To describe properly both short and long-term behavior of concrete undergoing thermal loadings, many researchers have highlighted the importance of coupled models involving heat conduction, liquid and gaseous water flow, and interactions of these fluid phases with the solid skeleton (see e.g. [1,2]). Traditionally, a Biot-like formulation is employed to reproduce such solid-fluid interactions, leading to complex non-linear coupled systems of equations (e.g. [3–6]). The dependence of transport and hydromechanical parameters on cracking is also of great importance and has been investigated in the case of brittle materials for example by [7,8] by means of damage variables. However, taking into account the detrimental effects of cracking on these physical properties introduces further non-linearity and increases both calculation times and convergence problems in the numerical simulations. In addition, in the case of partially saturated materials (which are typical conditions for the applications considered in this study), the saturation degree S_l is known to play an important role in the mechanical behavior via

* Corresponding author. Tel.: +33 1 6908 2383; fax: +33 1 6908 8441.
E-mail address: benoit.bary@cea.fr (B. Bary).

0017-9310/$ - see front matter © 2007 Elsevier Ltd. All rights reserved.
doi:10.1016/j.ijheatmasstransfer.2007.09.021

Nomenclature

a	radius of the ellipsoids
b	Biot coefficient
b^*	Biot coefficient in saturated conditions
c	heat capacity of concrete
d	water released in the porosity due to dehydration
$f_i(r)$	pore size function characterizing the ith pore class
h	thermal convection coefficient
h_r	relative humidity
k	bulk modulus
k_c	permeability of microcracks
k_s	bulk modulus of the solid phase
k_{ei}	permeability coefficient of phase i
k_{mi}	permeability to phase i of the matrix
k_{ri}	relative permeability of phase i
m	parameter of the damage evolution law
m_{ds}	mass of dry solid phase (cement and aggregate)
m_i	mass per unit material volume of phase i
p_c	capillary pressure
p_l	pressure of the liquid phase
p_{vs}	saturation vapor pressure
$\boldsymbol{q}$	heat flux
$\bar{r}$	mean curvature radius of the gas–liquid interface
s_i	entropy of phase i
s_{ds}	entropy of the dry solid phase
t	thickness of the adsorbed water layer
$\boldsymbol{v}_l$	velocity of phase i
$\boldsymbol{w}_i$	mass flux of phase i
$\boldsymbol{A}$	strain localization tensor
C_{pi}	mass heat capacity of phase i
C_{ds}	heat capacity of dry solid phase
H	Heaviside function
$\boldsymbol{I}$	second order identity tensor
$\boldsymbol{J}$	deviatoric projection operator
$\boldsymbol{K}$	intrinsic permeability tensor
$\boldsymbol{L}$	hydrostatic projection operator
$L_{l\to v}$	heat of vaporization
$L_{s\to l}$	heat of dehydration
M_v	molar mass of water
N	microcrack density number
$\overline{R}_i$	average radius of the pore class i
S_l	saturation degree
S_{lp}	saturation degree at which microcracks are emptied and pores are filled by water
T	current temperature
$V(r)$	cumulative volume of accessible pores having radii $r' > r$
ϕ_i	pore volume associated with the pore class i
$V_i(r)$	volume of size distribution function i
X	aspect ratio of the ellipsoids
α	coefficient of thermal expansion
α_s	coefficient of thermal expansion of solid phase
$\boldsymbol{\varepsilon}$	strain tensor
ε	bulk strains
ε_s	bulk strains of the solid phase
ε_0	initial strain threshold
ϕ	total porosity
ϕ_0	initial total porosity
ϕ_c	crack-induced porosity
ϕ_{cc}	volume fraction of inclusive phase corresponding to the percolation threshold
ϕ_d	fraction of the porosity due to dehydration of the solid phase
ϕ_l	fraction of the porosity occupied by water
λ	thermal conductivity
η_i	dynamic viscosity of the phase i
μ	shear modulus
$\mu_{l\to v}$	rate of evaporation of water per unit volume
ρ	microcrack density parameter
ρ_i	density of the water in phase i
$\boldsymbol{\sigma}$	stress tensor
σ	bulk stress
σ_s	bulk stress of the solid phase
σ_{gl}	gas–liquid interfacial tension
ξ_p	saturation level of porosity
ξ_c	saturation level of microcracks
ω	water mass loss
$\boldsymbol{\Theta}$	contact angle between the gas–liquid interface and the solid phase

the interaction Biot tensor (e.g. [9]), and in mass transfer of water. In this latter case both gaseous and liquid transport properties are indeed strongly affected by the quantity of water present in the pores, which depends mainly on capillary pressure, temperature and material microstructure. In practice, the experimentally obtained isotherm adsorption curves usually provide a macroscopic measure of S_l as a function of the relative humidity and for a given temperature, and integrate various phenomena occurring at the microscopic scale, as capillary condensation, surface tension and disjoining pressure (see e.g. [10,11]).

In this study we focus on the thermo-hydro-mechanical behavior of concrete subjected to temperature increases up to 150–200 °C, with possible different heating rates. In the literature, several physically well founded coupled models are available for such purposes, which are characterized by a complex set of equation to solve. The questions addressed here are as follows. Given the complexity of the coupled THM problem applied to concrete, we investigate the ability of simplified models to produce satisfying results when compared to experimental data, with a special regard to water mass transfers which play a crucial role in

the transient phase in the case of moderate heating. By transient phase, we mean the stage where both temperature and induced hydric gradients, which are known to possibly generate cracking, are important. It is indeed expected that when quasi-permanent conditions are achieved in terms of temperature and hydric changes, then the material does not experience additional detrimental phenomena, with the exception of creep and other long-term processes which are out of the scope of this work. In this study, the effects of isotropic damage are also evaluated and introduced in the mechanical and transfer parameters and their impact on macroscopic behavior analyzed, so as to verify the interest of such a development relating to mass transfers and to the particular loading cases considered. A simplified coupled model is developed to this aim on the basis of the mechanics of partially saturated porous media. The main simplification consists in assuming that the gaseous phase is composed uniquely of vapor. This assumption permits to combine the two initial mass conservation equations of water in liquid and gaseous phase into a single one, leading to considerably reduce the system of equations. Dehydration of the solid phase due to temperature increase and associated release of water in the porosity are considered. The constitutive equation for the skeleton relies on the concept of effective stresses in which only the (negative) liquid phase pressure is supposed to interact with the solid phase via the Biot coefficient. Tension-induced cracking is introduced in the model by means of an isotropic damage model where microcracks are represented by randomly oriented penny-shaped ellipsoids. Estimations of the mechanical, hydro-mechanical and transport parameters are obtained as a function of the saturation degree and damage by applying effective medium approximation schemes. The isotherm adsorption curves are supposed to evolve with temperature (which modifies physical properties as water density and gas–liquid interfacial tension) and damage (which provokes additional porosity). The governing equations are solved with the finite element method in the Cast3m code. The model is applied to the simulation of concrete cylinders behavior with height and diameter of 0.80 m subjected to heating rates of 0.1 and 10 °C/min up to 160 °C; the results are analyzed and compared with available experimental data. A numerical study on the role of the main hygromechanical parameters reveals that some coupled terms in the governing equations may be neglected, and that some parameters have a far larger impact on the results than other ones.

2. Modeling

2.1. Mechanical behavior

The developments presented in this section are an abridged version of the modeling formulation given in [12]; the reader is invited to refer to these works for more details. In particular, the introduction of an isotropic micromechanics-based damage variable and its effects on the main mechanical and transfer parameters are only briefly presented in the sequel, and emphasis is given on the concepts, assumptions and principal results. The mechanical behavior of the material is classically expressed by adapting the Biot formulation to the unsaturated condition case (see e.g. [1–3]). Only infinitesimal transformations are considered. It is supposed to simplify that the interaction of the gaseous phase and the skeleton is negligible relative to the one of the liquid phase. This assumption is equivalent to considering that the capillary pressure p_c results essentially from the liquid phase pressure p_l, i.e. $p_c \approx -p_l$. It may be justified in partially saturated conditions since the capillary pressure reaches typically several tens of MPa, and even much more for lower saturation degree S_l, according to the Kelvin's law (see Eq. (14)). The capillary pressure is then theoretically much greater than the one of the gaseous phase for S_l lower than about 0.9. The stress tensor $\boldsymbol{\sigma}$ is expressed as:

$$\boldsymbol{\sigma} = 2\mu \boldsymbol{J} : \boldsymbol{\varepsilon} + 3k\boldsymbol{L} : \boldsymbol{\varepsilon} - b\boldsymbol{I}p_l - 3\alpha k\theta \boldsymbol{I} \tag{1}$$

where $\boldsymbol{\varepsilon}$ is the strain tensor, $\boldsymbol{L}$ and $\boldsymbol{J}$ are projection operators such that $\boldsymbol{L} = 1/3\boldsymbol{I} \otimes \boldsymbol{I}$ and $\boldsymbol{J} = \boldsymbol{I}\overline{\otimes}\boldsymbol{I} - \boldsymbol{L}$ with $\boldsymbol{I}$ the second order identity tensor, μ and k the shear and bulk moduli in isothermal drained conditions, b the Biot coefficient, α the coefficient of thermal expansion, and $\theta = T - T_0$ with T and T_0 the current and initial temperatures, respectively. The bulk stress $\sigma = 1/3(\boldsymbol{I} : \boldsymbol{\sigma})$ is related to the bulk stress of the solid phase $\sigma_s = 1/3(\boldsymbol{I} : \boldsymbol{\sigma}_s)$ with $\boldsymbol{\sigma}_s$ the stress tensor of the solid phase, by (see e.g. [2]):

$$\sigma = (1-\phi)\sigma_s - \phi_l p_l, \quad \sigma_s = k_s\varepsilon_s - 3\alpha_s k_s \theta \tag{2}$$

in which $\varepsilon_s = \boldsymbol{I} : \boldsymbol{\varepsilon}_s$ with $\boldsymbol{\varepsilon}_s$ the strain tensor of the solid phase, k_s and α_s are the bulk modulus and thermal expansion coefficient of the solid phase, respectively, and ϕ and ϕ_l designate the total porosity and its fraction occupied by water (such that $\phi_l = S_l\phi$), respectively. These relations will be helpful to derive the mass conservation equation for the water in the next section. In the same spirit, it is also useful to express the evolutions of the porosity as a function of the bulk strains ε_s and $\varepsilon = \boldsymbol{I} : \boldsymbol{\varepsilon}$. It appears then necessary to introduce the porosity fraction due to dehydration of the solid phase, $\phi_d(T)$, consecutive to a temperature increase (see e.g. [13]). Likewise, the porosity $\phi_c(\rho)$ caused by microcracks opening has also to be taken into account, where ρ is the microcrack density parameter (see next subsection). Extending the approach of [2] with ϕ_0 the initial total porosity, the following results are obtained for ϕ in both explicit and incremental form:

$$(\phi - \phi_0 - \phi_d - \phi_c) = (1 - \phi + \phi_d + \phi_c)\boldsymbol{\varepsilon} - (1-\phi_0)\boldsymbol{\varepsilon}_s \tag{3}$$

$$\mathrm{d}\phi = (1-\phi)\,\mathrm{d}\boldsymbol{\varepsilon} - (1-\phi_0)\,\mathrm{d}\boldsymbol{\varepsilon}_s + \phi'_d\,\mathrm{d}T + \phi'_c\,\mathrm{d}\rho \tag{4}$$

2.1.1. Damage model

We briefly expose in the sequel the bases of the damage formulation used for estimating the effects of microcracks on the main mechanical and transfer parameters; a detailed presentation of the model is given in [12]. The proposed

isotropic damage model relies on a micromechanical approach, in which all types of microdefects are represented by penny-shaped ellipsoids. Such approaches are not new and have served to estimate the mechanical parameters of microcracked media (see e.g. [14,15]), and have also been applied to the case of porous media for example by [16,17]. For this latter case, one of the main interests is that the hydromechanical parameter can be also evaluated by means of the approximation scheme used for estimating the mechanical ones. Adopting such well-defined damage description allows then to conserve certain uniformity when estimating various physical properties (mechanical as well as transport ones). Here we choose a single scalar damage variable interpreted as an isotropic representation, by means of penny-shaped ellipsoids, of all types of micro (and macro)-defects induced by cracking.

In this study, concrete is viewed as a porous material composed of a homogeneous matrix in which are dispersed spherical inclusions representing porosity, and penny-shaped ellipsoids describing microcracks. These two families of inclusions are supposed to have well separated dimensions in typical conditions. For example, capillary pores are commonly defined as those 'large' pores with size greater than 0.1–1 μm up to a few hundred of μm (while pores of lower size are designated as inter and intra hydrates pores), which is assumed much smaller than the ellipsoids radius for moderate damage states. We also suppose that they are connected such that both gaseous and liquid phase are subjected to the same pressures in the two inclusion families. We assume to simplify that the ellipsoids are identical and randomly oriented, this latter assumption being necessary to comply with the isotropy condition. The ellipsoid distribution is classically characterized by the density $\rho = Na^3$, with N the density number and a the radius of the ellipsoids. Denoting as $2c$ the crack opening (dimension of the ellipsoid in the revolution axis direction), the volume fraction of microcracks is then $\phi_c = 4\pi/3\rho X$, with $X = c/a$ the aspect ratio of the ellipsoid. Since we consider two classes of inclusions with average size difference of several orders of magnitude, we adopt a two-steps homogenization procedure to estimate the effective physical properties (see Fig. 1). The first stage is formed by the porosity and the concrete solid phase, whereas the second step consists in the homogeneous phase resulting from the first stage, in which are randomly dispersed the penny-shaped inclusions. We choose to apply the interaction direct derivative (IDD) scheme developed by Zheng and Du [18] to estimate the mechanical and hydro-mechanical properties. This scheme has the advantages to be explicit and quite simple, and to not violate in certain circumstances the Hashin–Shtrikmann bounds contrary to the widely used Mori–Tanaka (MT) scheme (see e.g. [19]). The detailed calculations leading to the estimation of the mechanical parameters k^{IDD} and μ^{IDD} for open microcracks may be found in [12]; the results are given by:

$$\frac{k^{\mathrm{IDD}}}{k_s} = \left(1 + \frac{\phi_p T_p^h}{1-\phi_p}\right)^{-1}\left(1 + \frac{\rho\alpha_I^h}{1-\rho\alpha_{II}^h}\right)^{-1},$$
$$\frac{\mu^{\mathrm{IDD}}}{\mu_s} = \left(1 + \frac{\phi_p T_p^d}{1-\phi_p}\right)^{-1}\left(1 + \frac{\rho\alpha_I^d}{1-\rho\alpha_{II}^d}\right)^{-1} \tag{5}$$

where T_p^h and T_p^d are the hydrostatic and deviatoric parts, respectively, of the isotropic (dilute) strain localization tensor $\boldsymbol{T}_p^s = \left(\boldsymbol{I}^{(4)} - \boldsymbol{\Sigma}_p^s\right)^{-1}$, with $\boldsymbol{\Sigma}_p^s$ the Eshelby tensor of a spherical inclusion in the solid matrix and $\boldsymbol{I}^{(4)}$ the fourth order identity tensor; α_I^h, α_{II}^h, α_I^d and α_{II}^d are coefficients resulting from an average procedure over all possible orientations of microcracks (see [12] for further details).

2.1.2. Estimation of the Biot coefficient

The evaluation of the Biot coefficient is based on the consideration that the macroscopic stress $\boldsymbol{\sigma}_i$ generated by any microscopic homogeneous eigenstresses (or strain-free stresses) $p_i\boldsymbol{I}$ acting in the inclusion family i reads (see e.g. [17,20]):

$$\boldsymbol{\sigma}_i = -\langle {}^T\boldsymbol{A} : p_i\boldsymbol{I}\rangle = -\phi_i\langle {}^T\boldsymbol{A} : p_i\boldsymbol{I}\rangle_i = -\phi_i^T\boldsymbol{A}_i : \boldsymbol{I}p_i \tag{6}$$

where $\boldsymbol{A}$ is the strain localization tensor, $\langle\cdot\rangle$ and $\langle\cdot\rangle_i$ denote the average operations over the whole volume and the volume of phase i, respectively, and $\boldsymbol{A}_i = \langle\boldsymbol{A}\rangle_i$. We apply this equation to the case of our porous material subjected to the pore pressure p_l in the volume fraction ϕ_l; indeed

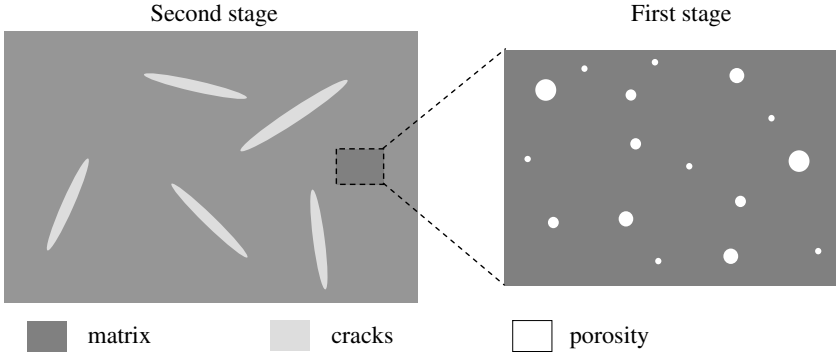

Fig. 1. 2D sketch of the two-step homogenization procedure.

p_l can be interpreted as an eigenstress which develops in the inclusions formed by the space occupied by water. To evaluate ϕ_l, we suppose that the same water pressure p_l exerts in the two inclusion families of the material. We further adopt the hypothesis that the microcracks first totally desaturate before porosity begins to empty in the case of desaturation from saturated state. Conversely, the microcracks are supposed to resaturate after porosity in the case of an imbibition process. With these definitions and assumptions, the effective Biot coefficient b is obtained in the form [12]:

$$b = \frac{\rho\alpha_I^h(1+\phi_p(T_p^h-1))\xi_c + \phi_p T_p^h(1-\rho\alpha_{II}^h)\xi_p}{(1+\phi_p(T_p^h-1))(1+\rho\alpha_I^h-\rho\alpha_{II}^h)} \tag{7}$$

where ξ_p and ξ_c are coefficients varying from 0 to 1 and indicating the saturation level of porosity and microcracks, respectively. They are defined as:

$$\xi_c = \left[\left(1+\frac{\phi_p}{\phi_c}\right)S_l - \frac{\phi_p}{\phi_c}\right]H(S_l - S_{lp}),$$
$$\xi_p = \left(1+\frac{\phi_c}{\phi_p}\right)S_l\big(1-H(S_l-S_{lp})\big) + H(S_l-S_{lp}) \tag{8}$$

where $S_{lp} = \phi_p/(\phi_c+\phi_p)$ corresponds to the saturation degree at which microcracks are emptied while pores are filled by water, and H is the Heaviside function.

It appears from Eq. (7) that for undamaged material ($\rho = 0$), b varies linearly with S_l as $b = b^* S_l$, where b^* is the Biot coefficient in saturated conditions. For damaged material, b is a bilinear function of S_l; the bifurcation point at which the microcracks are totally emptied and the pores totally filled with water corresponds to $S_l = S_{lp}$. It should be noticed that the evolutions of b as proposed here do not take into account the surface effects associated with disjoining pressure and surface tension which dominate in very fine pores (<5 nm). These effects may become important for lower saturation degree levels, and may lead to significant deviation from linearity in this domain (see e.g. [21]).

2.2. Governing equation for the water

2.2.1. Mass conservation equation

As water is present in both liquid and vapor form, the mass conservation of water includes necessarily, for general situations, 2 equations which take classically the form:

$$\frac{\partial}{\partial t}(m_l) = -\nabla\cdot(m_l \boldsymbol{v}_l) - \mu_{l\to v} + \dot{d},$$
$$\frac{\partial}{\partial t}(m_v) = -\nabla\cdot(m_v \boldsymbol{v}_v) + \mu_{l\to v} \tag{9}$$

in which $m_l = \phi(d)\rho_l(T,p_l)S_l$ and $m_v = \phi(d)\rho_v(T,p_v)(1-S_l)$ designate the mass per unit material volume of liquid water and vapor, respectively, with ρ_i the density of the water in phase i, $i \in \{l, v\}$ for liquid and vapor; $\mu_{l\to v}$ is the rate of evaporation of water per unit volume; $\boldsymbol{v}_i$ is the velocity of phase i and $\dot{d}$ is also a source term representing the rate of water released in the porosity due to dehydration. This latter quantity may be related to the mass of solid skeleton m_s through:

$$\frac{\partial m_s}{\partial t} = -\dot{d} \tag{10}$$

Combining Eqs. (9a) and (9b), we obtain:

$$(S_v\rho_v + S_l\rho_l)\frac{\partial\phi}{\partial t} + \phi\left(\rho_l\frac{\partial S_l}{\partial t} + \rho_v\frac{\partial S_v}{\partial t} + S_l\frac{\partial\rho_l}{\partial t} + S_v\frac{\partial\rho_v}{\partial t}\right) + \nabla\cdot(\boldsymbol{w}_l+\boldsymbol{w}_v) + \phi(S_v\rho_v+S_l\rho_l)\frac{\partial\varepsilon}{\partial t} = \dot{d} \tag{11}$$

where $\boldsymbol{w}_i = \rho_i\phi S_i(\boldsymbol{v}_i - \boldsymbol{v}_s)$ stands for the mass flux of phase i, with $\boldsymbol{v}_s$ the velocity of the solid phase; in Eq. (11), use is made of the classical simplification $\nabla\cdot(\boldsymbol{v}_s) \approx \partial\varepsilon/\partial t$ [4]. As mentioned in the introduction, it is assumed that the gaseous phase is only composed of vapor. This permits to largely simplify the model since the dry air which is initially mixed with vapor in this gaseous phase is totally neglected. As a consequence, no mass conservation for this constituent is required. According to the authors, several points may justify this hypothesis. First, the initial quantity of dry air present in the material is small, since typical saturation degree of concrete is generally greater than 0.9–0.95. Then, when temperature increases, evaporation augments and the vapor produced becomes progressively dominant in the gaseous phase, and replaces the air as transfers take place. Second, it has been demonstrated that the major process governing transfer phenomena for weakly permeable materials in ambient temperature conditions is the migration of liquid phase due to capillary pressure gradients, while transfers in gaseous phase are quasi-negligible (see e.g. [22]). With this hypothesis, the main phenomenon controlling the transport of water in both liquid and vapor state is the fluid conduction, since no diffusion processes can occur in the gaseous phase composed of a single constituent. Then, classical Darcy's law are used for expressing $\boldsymbol{w}_i$:

$$\boldsymbol{w}_i = -\rho_i\frac{\boldsymbol{K}}{\eta_i}k_{ri}(S_l)\nabla p_i \tag{12}$$

where $\boldsymbol{K}$ is the intrinsic permeability tensor, k_{ri} and η_i are the relative permeability and the dynamic viscosity of the phase i, respectively. In the following, it will be supposed that $\boldsymbol{K}$ depends upon the considered phase. Indeed, experimental values of so-called 'intrinsic' permeability obtained with gas in typical conditions are commonly reported to be greater by up to two orders than the ones measured with water (see e.g. [23]). It may be justified at least partly by the fact that the water adsorbed on the pore walls has specific properties which differ significantly from the ones of the bulk water. In particular, its transport properties are considerably reduced; moreover, the adsorbed water layers lessen the pore and crack sizes subject to the water flux.

Another reason may reside in the fact that the drying procedure (generally carried out at about 100 °C) applied to the specimen before performing the gas permeability test may generate diffuse microcracks and initiate the dehydration of certain solid phases (in particular ettringite which becomes thermodynamically unstable above about 60 °C), and consequently may artificially increase the permeability value to gas with respect to the 'true' intrinsic permeability. For convenience, we denote k_{ei} the permeability coefficient such that $k_{ei}(S_l,\rho)\boldsymbol{I}=\boldsymbol{K}$. We suppose that permeability remains isotropic for the damaged material, and that it is not affected by crack closure and state of stresses.

Introducing Eq. (4) into Eq. (11) in which ε_s is eliminated with the help of Eqs. (1) and (2), we arrive at:

$$b^*\frac{\partial\boldsymbol{\varepsilon}}{\partial t}+\left[-\varpi\frac{\partial S_l}{\partial p_c}+\frac{b-\phi S_l}{k_s}+\frac{\phi}{\rho_{lv}}\left(S_l\frac{\partial\rho_l}{\partial p_l}+S_v\frac{\partial\rho_v}{\partial p_l}\right)\right]\frac{\partial p_l}{\partial t}+\frac{\Xi}{k_s}\frac{\partial\rho}{\partial t}+\frac{1}{\rho_{lv}}\nabla\cdot(\boldsymbol{w}_l+\boldsymbol{w}_v)+\left[\frac{\phi}{\rho_{lv}}\left(S_l\frac{\partial\rho_l}{\partial T}+S_v\frac{\partial\rho_v}{\partial T}\right)+\varpi\frac{\partial S_l}{\partial T}+\left(\phi_d'+3\alpha\frac{k}{k_s}-3\alpha_s(1-\phi)\right)\right]\frac{\partial T}{\partial t}=\frac{\dot{d}}{\rho_{lv}}\qquad(13)$$

in which $\rho_{lv}=S_l\rho_l+S_v\rho_v$, $\varpi=\phi(\rho_l-\rho_v)/\rho_{lv}-p_l/k_s(\phi-\partial b/\partial S_l)$, and $\Xi=p_l\partial b/\partial\rho-(\varepsilon-3\alpha\theta)\partial k/\partial\rho+\phi_c'+\varpi k_s\partial S_l/\partial\rho$. In Eq. (13), it is implicitly supposed that S_l varies as a function of p_c, T and ρ, $\partial k_s/\partial T=0$, $k_s\gg\sigma_s-p_l$. As already mentioned, the function $S_l(p_c,T,\rho)$ integrates a high level of microstructural information in terms of pore size distribution and connectedness. In practice, it is more encountered in the form $S_l(h_r,T,\rho)$, where $h_r=p_v/p_{vs}$ is the relative humidity and p_{vs} the vapor pressure at saturation, for the reason that this latter can be determined by a simple (while time-consuming) experimental procedure. The Kelvin's law permits to carry out this change, though it is known that for lower h_r values this relation may be inappropriate due to dominating surface tension and disjoining pressure effects (see e.g. [3,24]). To simplify and because of the lack of precise information in this range of relative humidity, the Kelvin's law will be utilized in this study:

$$p_c=-\rho_l\frac{RT}{M_v}\ln h_r\qquad(14)$$

where M_v is the molar mass of water.

2.2.2. Estimation of the permeability to gas and water

We now proceed to estimate the permeability coefficients k_{ei} of the material as a function of the damage state represented by a given microcrack density and saturation degree. We adopt the simple approach based on the self-consistent scheme and initially proposed by [25]. This approach, called Generalized Effective Media (GEM) formulation, takes advantage of the well-known percolation feature of the self-consistent scheme, and introduces two adjusting parameters for characterizing the percolation threshold and the exponent in the percolation equation. It has been used to assess transport properties in problems of conduction, diffusion and permeability, although it is known that the resulting estimates may violate the Hashin–Shtrikman bounds in certain situations depending on the parameter values (see e.g. [26]). In this study, verifications have been made to make sure that these bounds are respected. The basic implicit equation of the GEM for two-phase media reads [25]:

$$\frac{\phi_i(\Sigma_i-\Sigma_e)}{\Sigma_i+\chi\Sigma_e}+\frac{(1-\phi_i)(\Sigma_m-\Sigma_e)}{\Sigma_m+\chi\Sigma_e}=0\quad\text{with }\chi=\frac{\phi_{cc}}{1-\phi_{cc}}\qquad(15)$$

In this relation, $\Sigma_j=\sigma_j^{1/t_e}$ with σ_j the transport property of phase j ($j=i,m$ and e stands for inclusion phase, matrix and effective medium, respectively), t_e is the percolation exponent and ϕ_{cc} is the volume fraction of inclusive phase corresponding to the percolation threshold. These last two quantities are considered as adjustable parameters. The classical self-consistent scheme for two-phase media composed of spherical particles is recovered when $t=1$ and $\phi_{cc}=2/3$. Applying such approximation scheme to estimate the permeability requires additional assumptions regarding the flow process in the penny-shaped ellipsoidal inclusions. Following [16] among others, we suppose that the flow in the microcracks can be approximated by a Poiseuille flow between two parallel plates separated by the distance $2c$. Let k_{ml} and k_{mg} designate the permeability to water and gas of the matrix composed of the solid phase and the porosity, and k_c the permeability of the cracks; we then have $k_c=c^2/3=(\rho/N)^{2/3}X^2/3$. k_{mj} corresponds to the permeability of the undamaged material and may be obtained experimentally for each fluid phase. The well-known function introduced by [27] is further used to modify the effective value of k_{ml} as a function of S_l, whereas the correction function proposed by [28] is adopted to adjust the one of k_{mg} (see Appendix A). Applying the GEM equation to the damaged material (step II of the homogenization procedure in Fig. 1) and retaining the scenario describing the saturation and desaturation process of microcracks and porosity as proposed in Section 2.1.2, the following expressions for the permeability to liquid k_{el} and to gas k_{eg} are found:

$$k_{el}=\left[\frac{1}{2}\left(\alpha+\sqrt{\alpha^2+4(k_ck_{ml})^{1/t_l}[\xi_c\phi_c\chi+\chi(1-\xi_c\phi_c-(1-\xi_c)\phi_c(1+\chi))]}\right)\right]^{t_l}\qquad(16)$$

$$k_{eg}=\left[\frac{1}{2}\left(\alpha'+\sqrt{\alpha'^2+4(k_ck_{mg})^{1/t_g}[(1-\xi_c)\phi_c\chi+\chi(1-(1-\xi_c)\phi_c-\xi_c\phi_c(1+\chi))]}\right)\right]^{t_g}\qquad(17)$$

with $\alpha' = k_{mg}^{1/t_g}(1-\phi_c(1+\chi)) + k_c^{1/t_l}((1-\xi_c)\phi_c + \chi((1-\xi_c)\phi_c - 1))$, $\alpha = k_{ml}^{1/t_l}(1-\phi_c(1+\chi)) + k_c^{1/t_l}(\xi_c\phi_c + \chi(\xi_c\phi_c - 1))$, $\chi = \phi_{cc}/(1-\phi_{cc})$, t_l and t_g are the exponents of the percolation equation for the liquid and gas, respectively. The percolation threshold is difficult to evaluate, and is assumed here to correspond to the crack density $\rho_{cc} = 1$, and t_l and t_g are adjusted so that the maximal permeability increase due to damage does not exceed 4 orders of magnitude.

The permeability evolutions for both gas and water versus the saturation degree as given by the model are illustrated in Fig. 2 with the following values: $X = 1 \times 10^{-3}$, $\phi_p = 0.15$, $k_{mg}(S_l = 0) = 1 \times 10^{-16}$ m^2, k_{ml} $(S_l = 1) = 1 \times 10^{-2}$ $k_{mg}(S_l = 0)$ m^2, $t_l = 3$, $t_g = 3$. As expected, it is observed that the crack-induced increase of permeability to water appears for higher saturation degrees, that is, when water progressively saturates the microcracks. This increase is more marked and occurs on a larger saturation degree domain for higher values of damage variable. The impact of damage is comparatively more pronounced on the permeability coefficient to gas. Indeed, due to the hypothesis concerning the drainage of microcracks in the first stage of desaturation, this transport property significantly augments relative to the undamaged case when the volume fraction of emptied microcracks becomes greater than the percolation threshold.

2.2.3. Estimation of the isotherm adsorption curves

We propose in this section to estimate the isotherm adsorption curves $S_l(h_r, T, \rho)$ by incorporating basic microstructural information in terms of pore size distribution, and by taking into account the effects of temperature change on certain physical properties (in particular, T appears in the expressions of water density and gas–liquid interfacial tension). Such approach is already available for example in [11] where a 3D polydispersed overlapping sphere assemblage system is used to represent the porosity as measured by experimental techniques like mercury intrusion porosimetry (MIP). In this paper, a more simple description of the microstructure is retained, where the main pore size domains characterizing the cementitious materials are directly represented by appropriate normalized distribution functions. Moreover, it is supposed that the additional porosity consecutive to crack opening affects significantly the isotherm adsorption curves, and is introduced by means of a pore size domain centred on a much larger size than the greater one of the undamaged material. The effects such as ink bottle and pore-blocking (see e.g. [29]), leading in particular to hysteresis loops in the $S_l(h_r, T, \rho)$ curves when the material is submitted alternatively to adsorption and desorption (wetting–drying paths), are not considered in this study. The objective of this simplified approach is to introduce a more realistic representation of the adsorption curves than the classical curves $S_l(h_r)$ generally retained in coupled THM models. In particular, it is expected that the effects of microcrack porosity on the adsorption curves will be limited as the size domain of these microcracks corresponds to large meniscus radius and then to relative humidity near to 1. However, a better numerical resolution of the equations of the THM model requires for the mathematical representations of the adsorption curves to be continuous and their derivatives with respect to T and S_l to be also continuous, since they explicitly appear in the formulation. Let us define the function $f(r)$ which is generally employed to express the MIP results in the form:

$$f(r) = \frac{\partial V(r)}{\partial(\ln(r))} = r\frac{\partial V(r)}{\partial r}, \tag{18}$$

where $V(r)$ is the cumulative volume of accessible pores (in the sense of MIP process) having radii $r' \leqslant r$. In practice, $f(r)$ permits to emphasize the pore size domains which are dominant in the material. Due to the presence of multiple pore size classes in typical cementitious materials, we decompose $f(r)$ into $f(r) = \lambda_i f_i(r)$ with λ_i a positive scalar and $f_i(r)$ the pore size function characterizing the ith pore class. In this study we limit the number of classes to 3 (2 classes for the sound material and the third one for the crack-induced porosity), but additional classes may be considered without difficulty. Among the large diversity of size

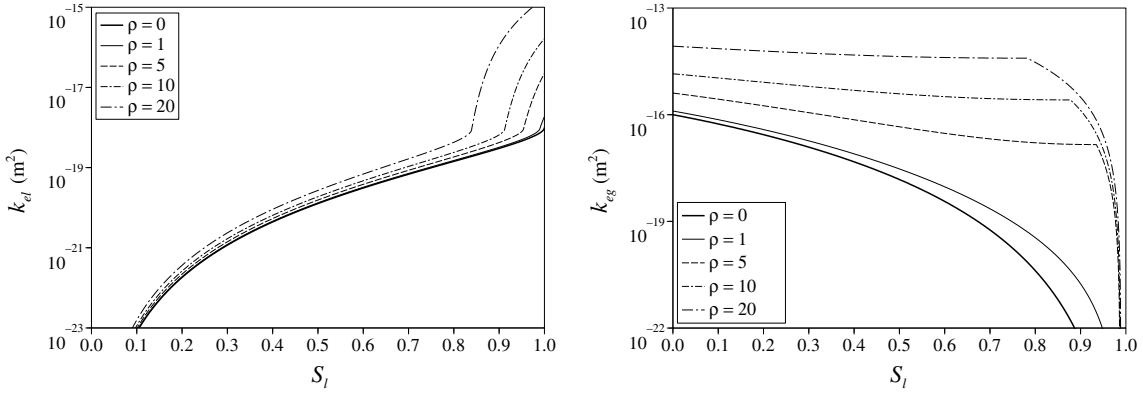

Fig. 2. Evolutions of the permeability coefficient for water (left) and for gas (right) as a function of saturation degree for different values of microcracks density parameter ρ.

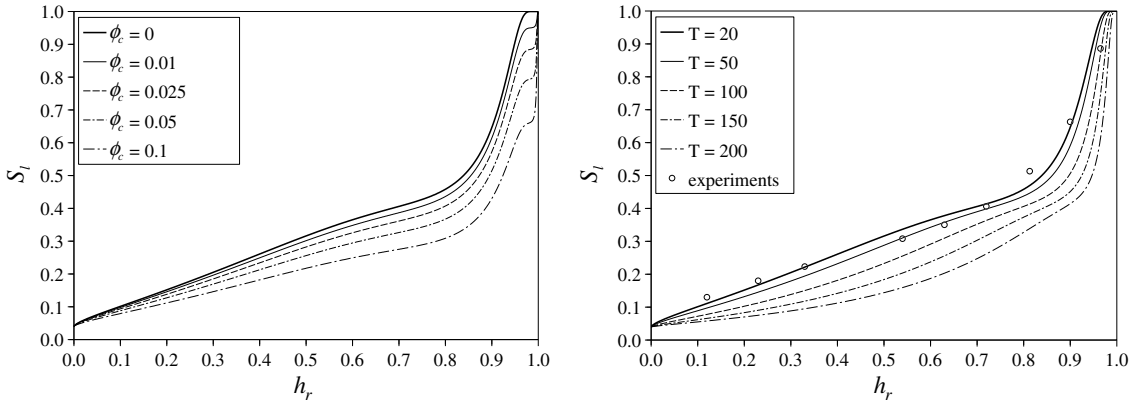

Fig. 3. Evolutions of the adsorption curves for different values of crack-induced porosity ϕ_c (left) and for different temperatures (right); experimental data at 20 °C for an ordinary concrete [24].

distribution functions proposed in the literature, we propose to use the Schulz distribution defined as (see e.g. [19]):

$$f_i(r) = \frac{1}{\Gamma(m_i+1)}\left(\frac{m_i+1}{\overline{R}_i}\right)^{m_i+1} r^{m_i}\exp\left(-\frac{m_i+1}{\overline{R}_i}r\right) \tag{19}$$

where $\Gamma(x)$ is the Gamma function, $\overline{R}_i$ is the average radius of the class i such that $\overline{R}_i = \langle R\rangle_i$ with $\langle X(R)\rangle_i = \int_0^\infty X(R)f_i(R)\,dR$. When the positive parameter m_i is limited to integer values, we have $\Gamma(m_i+1) = m_i!$; in the sequel this restriction will be adopted for the sake of simplicity. The distribution becomes sharper when m_i increases, and the limit case $m_i \to \infty$ corresponds to a monodisperse distribution. We further define the volume of size distribution function i as $V_i(r) = \int_0^r (f_i(R)/R)\,dR$, such that $V(r) = \lambda_i V_i(r)$. $V_i(r)$ is then the cumulative volume fraction of pores belonging to the class i and having a radius $r' \leqslant r$. With the simplification $m_i = m_f$ for all the pore classes, the following expression is obtained for $V_i(r)$:

$$V_i(r) = \frac{-\kappa_i}{m_f}\left[\exp(-\kappa_i r)\sum_{j=1}^{m_f}\frac{(\kappa_i r)^{j-1}}{(j-1)!} - 1\right] \tag{20}$$

with $\kappa_i = (m_f+1)/\overline{R}_i$. The saturation degree $S_l(r)$ corresponding to the volume fraction of pores with radius lower than r filled by water is simply expressed by $S_l(r) = V(r)/\phi$. Note that ϕ takes the following form:

$$\phi = V(r\to\infty) = \frac{\lambda_i\kappa_i}{m_f} \tag{21}$$

Denoting by ϕ_i the pore volume associated with the class i, we have $\phi_i = (\lambda_i\kappa_i)/m_f$ (without sum), and then the parameters λ_i may be identified by the relation:

$$\lambda_i = \frac{m_f\phi_i\overline{R}_i}{m_f+1}(\text{no sum}) \tag{22}$$

$\overline{R}_i$ are identified experimentally by exploiting for example the MIP results. For this approach to be applicable, it remains to connect the pore radius r to the variables h_r (or p_c) and T. This is done by appealing to the Kelvin's law (Eq. (14)) and to the Laplace equation given by $p_c = (2\sigma_{gl}\cos\Theta)/\bar{r}$, where σ_{gl} is the gas–liquid interfacial tension, Θ is the contact angle between the gas–liquid interface and the solid phase, and $\bar{r}$ is the mean curvature radius of the gas–liquid interface. It is generally assumed that $\Theta = 0$ for cementitious materials (see e.g. [30]), and the Laplace equation may be classically rewritten as

$$p_c = \frac{2\sigma_{gl}}{r-t} \tag{23}$$

where t is the thickness of the adsorbed water layer depending on the relative humidity h_r. Because of the presence of this adsorbed water layer (except when $h_r \approx 0$), the radius of the gas–liquid interface meniscus is obtained by reducing the pore radius by t, and then $\bar{r} = r - t$. From Eqs. (14) and (23), we have:

$$r = -\frac{2\sigma_{gl}M_v}{\rho_l RT\ln h_r} + t = \frac{2\sigma_{gl}}{p_c} + t \tag{24}$$

which permits to write explicitly $S_l(p_c,T,\rho) = V(p_c,T,\rho)/\phi$. In these relations, σ_{gl} and ρ_l are assumed to depend only on T, and t only on h_r; expressions based on experimental data and drawn from literature are given in Appendix A. The method is illustrated in Fig. 3 where $S_l(h_r,T,\rho)$ curves are presented for different values of crack-induced porosity ϕ_c (left), and for different temperatures up to 200 °C (right). The basic parameters of the model are set to the following values: $\overline{R}_1 = 1.8\times10^{-9}$ m, $\phi_i = 0.12$; $\overline{R}_2 = 20\times10^{-9}$ m, $\phi_2 = 0.07$; $\overline{R}_3 = 500\times10^{-9}$ m (this pore class corresponds to the crack-induced porosity), and $m_f = 3$, such that the adsorption curve corresponding to undamaged material at 20 °C is close to the one obtained experimentally for a similar ordinary concrete in [24] (Fig. 3 right). It is clear from Fig. 3 that both damage-induced porosity and temperature affect significantly the $S_l(h_r,T,\rho)$ curves. Whereas the impact of ϕ_c increases as a function of h_r, the effects of T appear more important for intermediate h_r (this last point is in accordance with [11]). Again, it is emphasized that the effects of damage on the adsorption curves may be at first glance viewed as a reduction by a certain factor of the initial curves, as the size domain of

damage porosity only affects the h_r range near 1. Nevertheless this permits to conserve a mathematically well-defined expression of $S_l(h_r, T, \rho)$ in the equation set of the THM model, which improves their numerical resolution. It will be shown in the numerical simulation section that taking into account these evolutions of S_l (h_r, T, ρ) (in particular those resulting from T) has a considerable influence on the results.

2.3. Heat equation

The entropy conservation equation is classically written in the form (see e.g. [2]):

$$T\left[\frac{\partial S}{\partial t} + \nabla \cdot (s_l \boldsymbol{w}_l + s_v \boldsymbol{w}_v)\right] = -\nabla \cdot \boldsymbol{q} \tag{25}$$

where $S = S_s + m_l s_l + m_v s_v$ is the total entropy of the system; S_s, s_l and s_v are the entropy of the solid skeleton, water and vapor, respectively; $\mathbf{q}$ is the heat flux. The state equations for the fluid and solid phases take the form:

$$s_l = s_{l0} + C_{pl} \ln \frac{T}{T_0}, s_v = s_{v0} + C_{pv} \ln \frac{T}{T_0} - R \ln \frac{p_v}{p_{v0}},$$
$$S_s = m_{ds} s_{ds} + (d_0 - d) s_{bw} \tag{26}$$

where C_{pl} and C_{pv} are the mass heat capacities of the free (bulk) water and vapor; m_{ds} is the mass of cement and aggregate per unit volume; $(d_0 - d)$ represents the total mass of bound water and s_{bw} its entropy; $s_{ds} = s_{ds0} + C_{ds} \ln(T/T_0)$ is the entropy of the dry solid phase with C_{ds} its heat capacity. Introducing these state equations into Eq. (25), we obtain:

$$c(S_l, d)\frac{\partial T}{\partial t} + (\boldsymbol{w}_l C_{pl} + \boldsymbol{w}_v C_{pv})\nabla T - \frac{\boldsymbol{w}_v}{\rho_v} \cdot \nabla p_v = -\nabla \cdot \boldsymbol{q} - L_{l\to v}\mu_{l\to v} - L_{s\to l}\dot{d} \tag{27}$$

where $c(S_l, d) = m_{ds} C_{ds} + \phi \rho_l S_l C_{pl} + \phi \rho_v (1 - S_l) C_{pv} + (d_0 - d) T C_{bw}$ is the heat capacity of concrete, and C_{bw} is the heat capacity of the bound water. $(\boldsymbol{w}_l C_{pl} + \boldsymbol{w}_v C_{pv})\nabla T$ and $\boldsymbol{w}_v/\rho_v \nabla p_v$ are the heat transported by fluid convection and heat dissipation due to the liquid phase compressibility, respectively, which are both negligible [31]. $L_{l\to v} = T(s_v - s_l)$ is the heat of vaporization and, by analogy, $L_{s\to l} = T(s_s - s_{bw})$ is the heat of dehydration [32]. The heat flux is classically expressed via the Fourier law as:

$$\boldsymbol{q} = -\lambda(S_l, d)\nabla T \tag{28}$$

with λ the thermal conductivity. Relations and values of the various parameters introduced in this section are given in Appendix A. Finally, the heat equation is rewritten as

$$c(S_l, d)\frac{\partial T}{\partial t} = \nabla \cdot (\lambda(S_l, d)\nabla T) - L_{l\to v}(T)\mu_{l\to v} - L_{s\to l}\dot{d} \tag{29}$$

3. Numerical simulations

3.1. BETHY experiments

The BETHY experiments were conceived with twofold objectives: to measure the water mass loss of a non-reinforced concrete structure (in this case the specimens have a size of the order of meter) during the test and to investigate the effects of a high heating rate on the behavior of this structure. This last aspect is envisaged keeping in mind the objective of investigating the structure response in the transient domain regarding mass transfers and temperature gradients. The fact that no external mechanical loading is applied allows focusing on the effects of thermo-hydric loadings and their mechanical consequences. The specimens consisted in concrete cylinders with height and diameter of 0.80 m (without steel reinforcement), with a mass of nearly 1000 kg (see Fig. 4 left). These specimens were instrumented so as to quantify in several points placed radially in the median plan (the plan perpendicular to the revolution axis at mid-height) the evolutions of temperatures and gas pressures (Fig. 4 right); moreover the mass loss of the whole structure was measured continuously. Gas pressure characterization is of interest as this parameter is suspected to be largely involved in phenomena linked to spalling, known to appear for moderate to high temperatures. The specimen were subjected to thermal loading consisting in a linear increase of the oven temperature from ambient to 160 °C, followed by a plateau at 160 °C up to about 160 h. Two heating rates were considered: 0.1 and

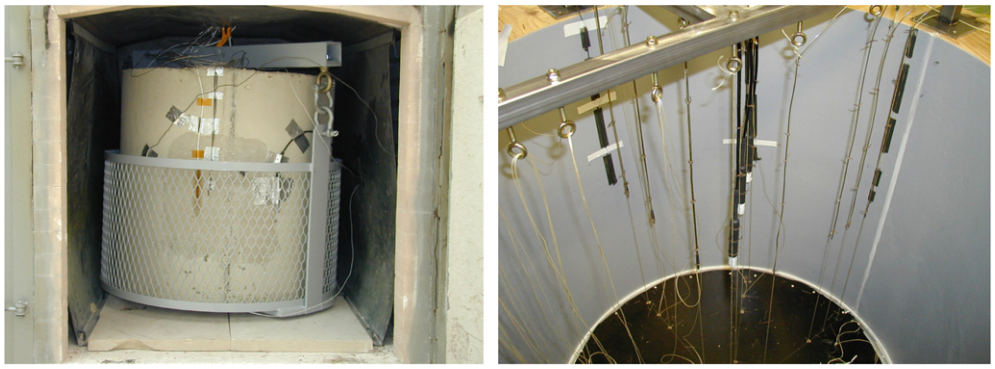

Fig. 4. Concrete cylindrical specimens (left) and sensors located inside the specimens before casting (right).

10 °C/min. The composition of concrete with w/c ratio of 0.62 is given in Appendix A. The water released during dehydration process was measured to $d = 0.39(T - 60) + 1.72$ (in kg/m^3) if $T \geqslant 60$ °C and $d = 0$ otherwise. The permeability to gas which evolves as a function of the temperature is directly expressed via the quantity of dehydrated water d. It has been estimated from measurements at ambient temperature after heating as: $k_{mg} = 1 \times 10^{-15}\exp(0.01d)$ m^2. The initial porosity obtained by mercury intrusion porosimetry is $\phi_0 = 0.19$. The Young modulus determined at ambient temperature after heating varies linearly from 26.5 GPa at 20 °C to 17.0 GPa at 160 °C. The experimental thermal conductivity for the totally desaturated material varies linearly from 2.3 to 1.9 W/m/°C between 60 and 160 °C. It is further assumed that the water released at 60 °C is only free water (and consequently dehydration is not initiated, in agreement with the test results) and the thermal conductivities at 20 °C and 60 °C are equal for the dry material. Then, the evolution of this parameter in partially saturated conditions is proposed as a function of S_l and d as $\lambda(S_l, d) = \lambda_{60} + [S_l/S_{l0}(\lambda_{20} - \lambda_{60})] - k_d d$, where $k_d = 9.83\times10^{-3}$ is the slope of the linear experimental curve $\lambda(S_l = 0, d)$, $\lambda_{60}(S_l = 0, d = 0) = 2.3$ W/m/°C and $\lambda_{20}(S_{l0}, d = 0) = 2.7$ W/m/°C. More details and some other useful parameters are given in Appendix A.

3.2. Simulation of the BETHY experiments

The model developed in Section 2 is applied to the simulation of the BETHY experiments. The equations of the model are solved iteratively and successively by means of the classical finite element method and an implicit scheme for the time space in the Cast3m code developed at CEA. Thermal loading is applied at the specimen surfaces via a convection condition, and a coefficient $h = 25$ W/m^2/K is retained in the study. This constant coefficient is adjusted so that the experimental temperature evolution measured at the nearest point from the surface is close to the simulated one. The constant vapor pressure $p_v = 3000$ Pa is prescribed at the sample boundary, and since the saturation vapor pressure augments with T, it leads to a decrease of h_r. This condition is equivalent to considering that the vapor which migrates and arrives at the specimen surface becomes in the same pressure state than the one of the ambient atmosphere (or that the corresponding convection coefficient is infinite). It is also similar to prescribing an evolution of h_r (or S_l) as a function of temperature. Recall that the vapor pressure inside the specimen may be here interpreted as an overpressure with respect to the initial atmospheric one. Simulations are carried out by using 8-node quadrilateral elements in 2D axisymmetrical formulation. Due to the symmetries of the structure and of the boundary conditions, only a quarter of it is considered in the computations. The boundary conditions and the mesh composed of 4900 elements are represented on Fig. 5. We present hereafter some of the numerical results obtained in the case of a heating rate of 0.1 °C/min from 30 to 160 °C. It is worth mentioning that the one-month period of drying following the specimen fabrication and preceding the test is simulated by imposing a temperature of 25 °C and a constant vapor pressure of 2500 Pa at the specimen surfaces. This permits to evaluate the non-homogeneous initial saturation degree and capillary pressure distributions inside the structure at the beginning of the heating stage. Homogeneous initial conditions for temperature (25 °C) and for relative humidity (0.96, corresponding to a saturation degree of about 0.92) are assumed at the onset of the drying phase. The simulated mass loss of water during the heating stage obtained by setting $k_{rl}(S_l = 1) = 1 \times$

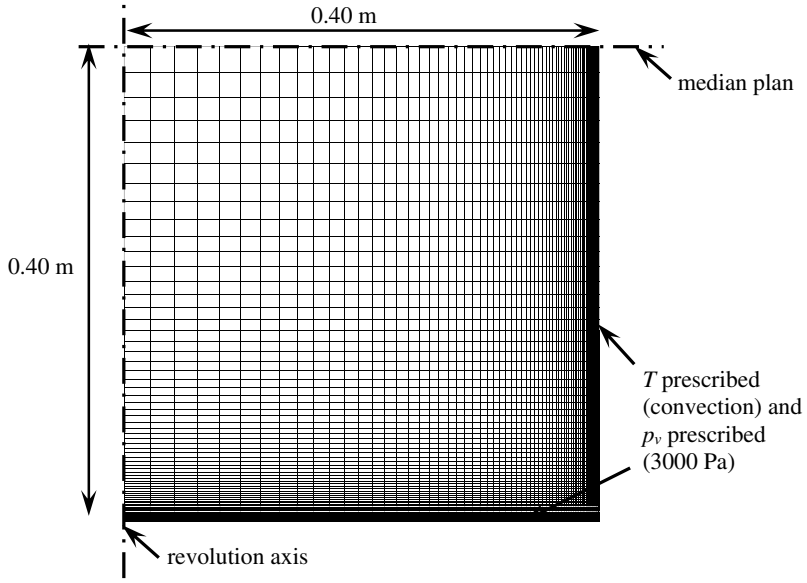

Fig. 5. Boundary conditions and mesh used for the computations.

$10^{-2} \times k_{mg}(S_l = 0)$ is depicted against time on Fig. 6, and is compared with experimental data for the whole structure. The expression of the water mass loss ω is given by:

$$\omega = (\rho_i \phi_i)_0 + d - (1 + \varepsilon)(\rho_i \phi_i) \quad \text{with } i = \{l, v\} \tag{30}$$

With this adjusted value of k_{ml} for $S_l = 1$, the numerical results appear to be in good agreement with experimental ones, except in the first hours of heating where they are somewhat overestimated. Note that the initial mass of the specimen is $\omega_0 = 981$ kg, and then the percentage of mass loss is simply given by $\omega/\omega_0 \times 100$.

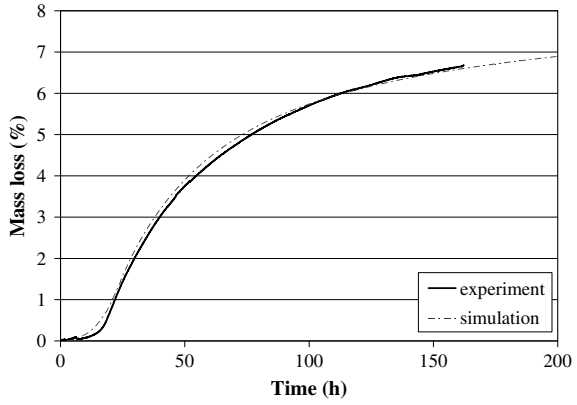

Fig. 6. Experimental and computational mass loss of water as a function of time for a heating rate of 0.1 °C/min.

On Fig. 7 are shown the computational evolutions of the temperature at different points located in the median plan of the specimen (near the surface (a), at $r = 0.35$ m (b), $r = 0.25$ m (c) and $r = 0.1$ m (d) from the revolution axis), and the corresponding experimental measures. It can be observed that the simulated temperatures are in good agreement with the experimental ones for the points situated near the surface of the specimen (note that the thermal convection coefficient has been adjusted for that purpose), whereas some differences appear for the points closer to the revolutions axis. The major distinctions occur after about 50 to 100 h, where the simulations systematically overestimate the temperatures. One reason could be that the specimen is severely damaged in this zone (as is corroborated by the numerical results, see Fig. 9), modifying the thermal properties of the material, and in particular the thermal conductivity. Another causes may be that the convection coefficient H varies with temperature, and that heating is not homogeneous due to the presence of the door oven (as indicated by the discrepancies between experimental data obtained for different points situated at the same distance from the revolution axis, see Fig. 7).

On Fig. 8 are shown the experimental and simulated gas pressures at the points situated at $r = 0.25$ m and $r = 0.1$ m from the center of the specimen median plan. The confrontation reveals that the numerical gas pressure for the point at $r = 0.25$ m is in relatively good accordance with experiments, whereas the simulations largely overestimate the

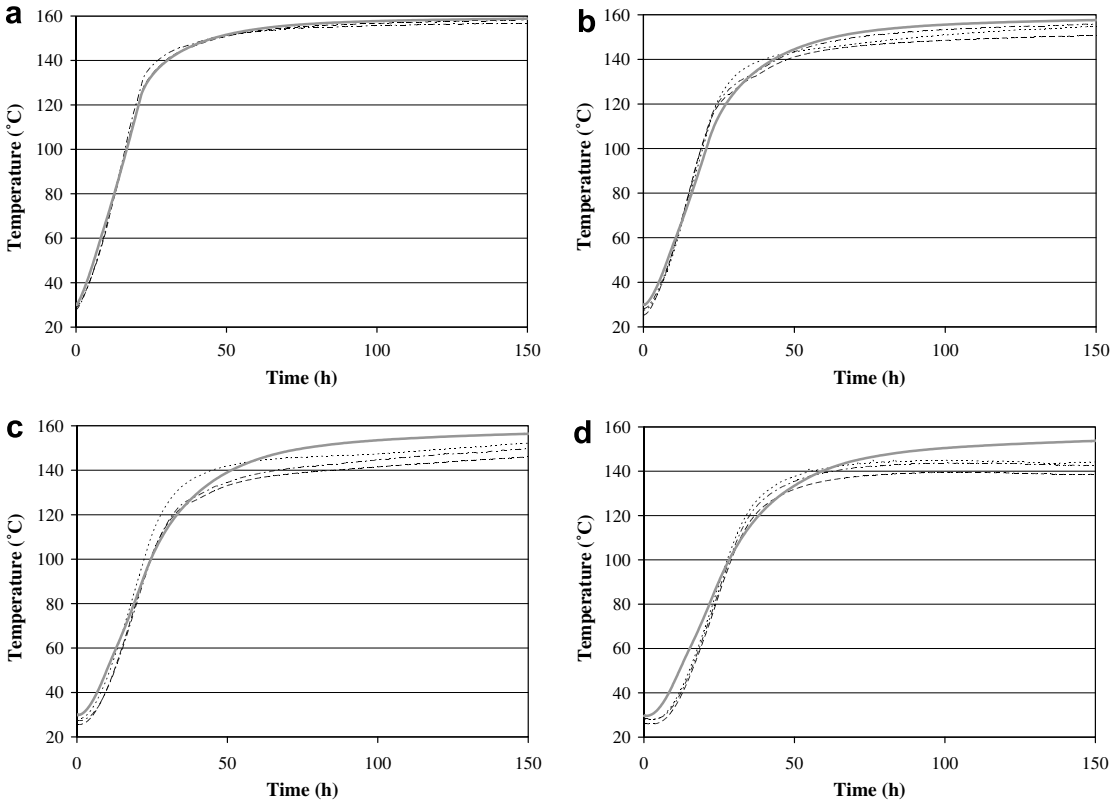

Fig. 7. Experimental (dashed and dotted lines) and computational (continuous gray line) evolutions of the temperature as a function of time for different points situated near the surface (a), at $r = 0.35$ m (b), $r = 0.25$ m (c) and $r = 0.1$ m (d) from the revolution axis in the median plan of the specimen.

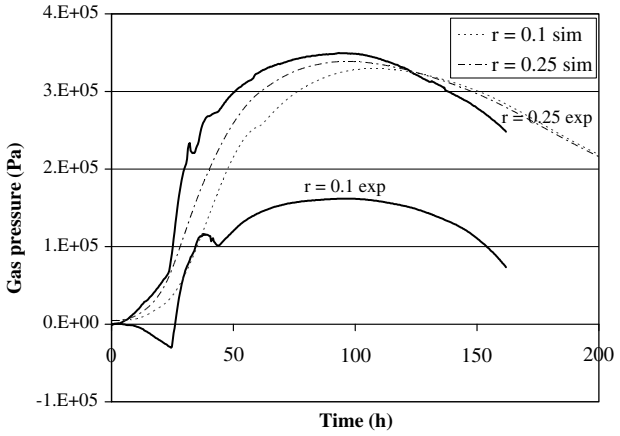

Fig. 8. Experimental and computational evolutions of the gas pressure as a function of time for the points situated at $r = 0.25$ m and $r = 0.1$ m from the revolution axis in the median plan of the specimen.

pressures at the other point. In this latter case it is worth mentioning that the experimental data may be criticized for exhibiting negative values; moreover, it can be observed a brusque decrease of the pressure at about 40 h, which may again be explained by the development of crack porosity which augments the volume accessible to gas and then may lessen its pressure. The model is not able to capture this feature but reproduces the reduction of saturation degree consecutive to this crack porosity growth. It should be noted that similar discrepancies between experiments and simulations are reported for example in [13] with the use of a more complete formulation describing water and gas transfers. Fig. 9 presents the damage pattern (left) and the Biot coefficient distribution (right) obtained at the end of the testing period (200 h). The specimen exhibits a significant cracking in its median plan, and in a lesser extent near its boundaries and along the revolution axis. A scrutiny of damage development shows that the main horizontal crack initiates in the vicinity of the revolution axis in the median plan at about 15 h, then kinks and propagates vertically near the surface at about 40 h up to nearly 80 h (the structure geometry implies that this vertical crack would take place all around the specimen); after this time this macrocrack does no more evolve. Obviously further experimental investigations would be necessary to validate such damage scenario. Whereas surface cracking can be attributed only to drying effects, internal damage results from the action of thermo-hydric gradients. More precisely, the main horizontal crack initiation is undoubtedly caused by the mechanical consequences of temperature gradients. Some verification has indeed proved the absence of positive pore pressure that would follow from a complete resaturation and capable to generate tensile stresses in the damaged zone. Moreover, drying effects tend to compress the central zone of the specimen and then reduce the tensile-induced stresses due to temperature gradients. The second phase of the main crack propagation (after its bifurcation) results from a combined action of both temperature and capillary pressure gradients. The former are less important than in the first stage due to more homogeneous temperatures, and the latter lead to considerable tensile stresses in the skeleton. Then, damage induced by both thermal and hydric loading appears to affect significantly the mechanical integrity of the structure. However, as no macrocracks reach the surface of the specimen, it is believed that their influence on the mass transfers is limited since no additional preferential paths for vapor and liquid migration are created (with the exception of the slight surface damage caused by drying). As expected, an important decrease of the Biot coefficient in both damaged and low saturated zones is observed in Fig. 9 (right). On the opposite, the higher values are located in the less desaturated and undamaged zones.

In order to study the influence of certain parameters on the results, several new simulations are carried out with the following configurations: the isotherm adsorption curve does not vary with temperature and damage ($S_l(h_r, T, \rho) \equiv S_l(h_r, T = 30\ ^\circ\mathrm{C}, \rho = 0)$, denominated 'Sl ini'), $X = 0$ (this case is equivalent to neglecting the crack-induced porosity), and the terms involving mechanics are removed from the mass conservation equation of water (designated as 'uncoupled'). We present the computational water mass loss and the gas pressure evolutions at $r = 0.25$ m from the center of the specimen obtained for these different con-

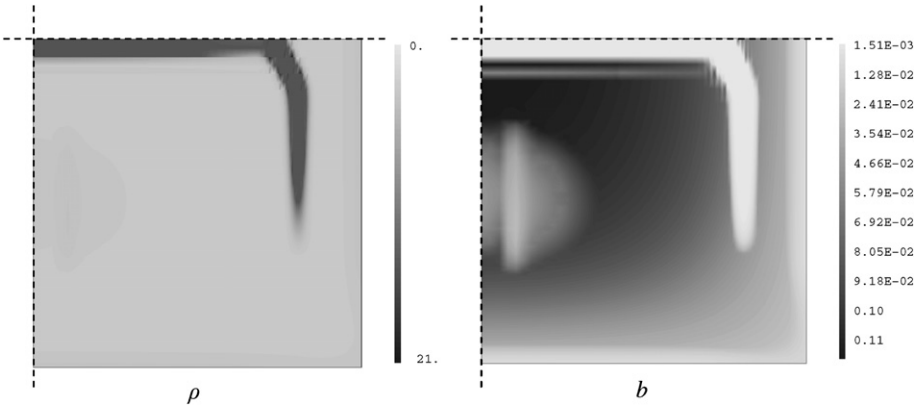

Fig. 9. Damage pattern (left) and Biot coefficient distribution (right) at 200 h.

figurations and the 'reference' one detailed previously in Figs. 10 and 11, respectively. The main conclusions which

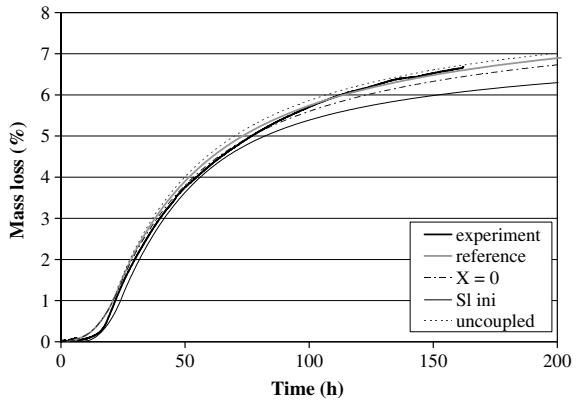

Fig. 10. Experimental and numerical mass loss of water in the following configurations: same parameters as in Fig. 6 ('reference'), $X = 0$, no effect of damage and temperature in the adsorption curve ('Sl ini'), no mechanical coupling in the mass conservation of water ('uncoupled').

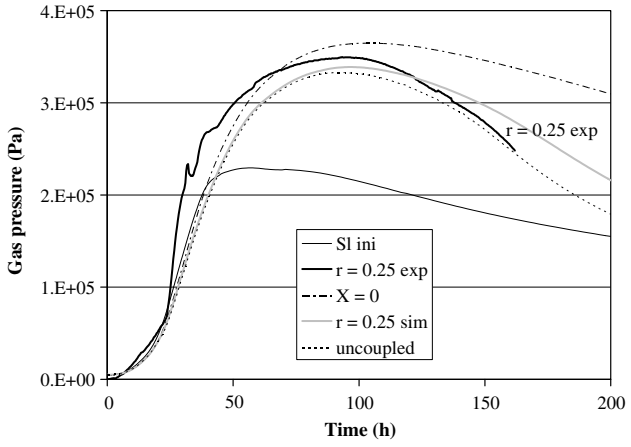

Fig. 11. Experimental and numerical gas pressure evolutions at $r = 0.25$ m in the following configurations: same parameters as in Fig. 6 ('reference'), $X = 0$, no effect of damage and temperature in the adsorption curve ('Sl ini'), no mechanical coupling in the mass conservation of water ('uncoupled').

can be drawn from the numerical results are as follows. All configurations give nearly the same water mass loss evolution except the case 'Sl ini' which differs significantly. The configurations 'Sl ini' and $X = 0$ affect importantly and moderately, respectively, the gas pressure evolutions with respect to the reference case. On the opposite, the 'uncoupled' configuration is very close to this reference case, which means that, given the uncertainties on some of the most influential parameters, the complexity introduced in the model when taking into account the mechanical coupling in the mass balance equation for water may be neglected. Conversely, the adsorption curve appears to be of great importance in the simulations and should then be carefully evaluated.

Finally, to close this study we present in Fig. 12a both computational and experimental (on two different specimens) evolutions of water mass loss obtained in the case of the heating rate of 10 °C/min up to 160 °C. Except this loading condition, all parameters are unchanged with respect to the case with the heating rate of 0.1 °C/min. The comparison shows a good agreement between experiments and simulations. Fig. 12b presents the numerical and experimental variations of temperature at 3 different points situated in the median plan of the specimen. Again, it is observed that the simulations overestimate the experimental temperatures after about 30–40 h. Last, Fig. 13 depicts the numerical evolutions of gas pressures as a function of time for the two heating rates considered in this study, and for several points in the median plan. It is observed that the differences between the two cases reside essentially in kinetics aspects, i.e. a faster increase and decrease of pressures with same maximal magnitude for the higher heating rate. Unfortunately, the gas pressure sensors have rapidly dysfunctioned and no experimental results are available for this loading case for a comparison with the simulations. Globally, the behavior of the specimen with a heating rate of 10 °C/min seems not to be fundamentally different from the one with 0.1 °C/min, as attested by numerical results and by experimental data.

To summarize the numerical results, in the case of the tested specimens and the considered temperature range,

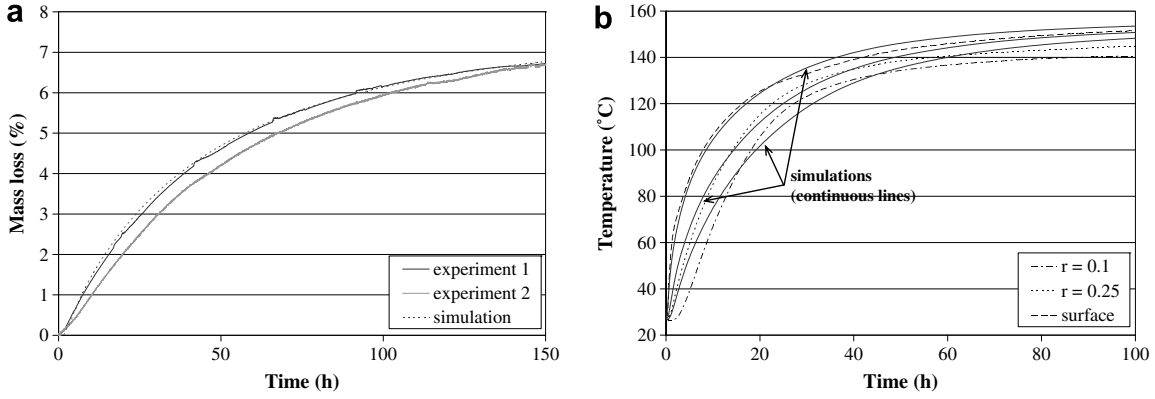

Fig. 12. Experimental and numerical water mass loss (a) and temperatures at different points situated in the median plan (b) for specimens subjected to a heating rate of 10 °C/min.

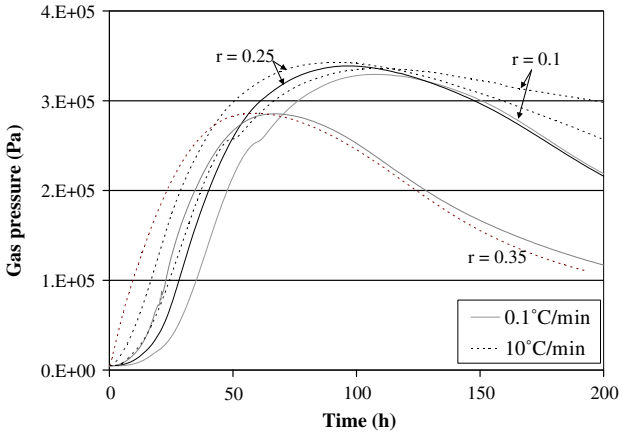

Fig. 13. Comparison of numerical gas pressures at different points located in the median plan of the specimens subjected to heating rates of 0.1 and 10 °C/min.

the interest of taking into account the consequences of damage on the various physical properties appears to be modest when the purpose is to characterize the mass transfers and the temperature response in the transient phase of thermal loading. Of course, the conclusion is different regarding the mechanical integrity of the structure, or in the case where the structure is subjected to pressurized gas loading. The simplified model (i.e. with only one mass conservation equation) seems to be able to correctly reproduce the major phenomena; a further simplification may even be incorporated by neglecting the mechanical term in the mass balance equation for water. Not surprisingly, the adsorption curves and their evolutions, in particular as a function of temperature, have a considerable impact on mass transfers in the transient phase of thermal loading. These curves then play an important role in the global THM behavior of concrete structures in such loading conditions, as the saturation degree is involved in numerous physical properties of the material.

4. Conclusions

This paper presents a simplified THM model capable of reproducing the main features of the thermo-hydric behavior in the transient phase of concrete subjected to moderate heating. The simplification resides in the fact that the gaseous phase is assumed to be composed only of vapor, which allows to combine the two mass conservation equations for water and vapor into a single one. An isotropic damage model relying on a microcrack description by means of randomly oriented penny-shaped ellipsoids is introduced and permits to estimate the mechanical parameters, Biot coefficient and permeability evolutions as a function of damage and saturation degree. The model is applied to the simulation of large concrete specimens subjected to heating rates of 0.1 and 10 °C/min up to 160 °C. Numerical results appear to be in relatively good agreement with experimental ones in terms of water mass loss and temperatures, and reproduce qualitatively the evolution of gas pressures as a function of time.

A numerical study reveals that the adsorption curve affects importantly the results; in particular, its dependence upon temperature and to a lesser extent crack-induced porosity should be precisely taken into account. On the opposite, the mechanical coupling terms appearing in the mass balance equation of water seem to have only a minor impact on the results and, given the complexity they introduce in the model and the uncertainties regarding other more influential parameters, they may be neglected in practice. The damage effects on the thermo-hydric behavior of the considered structure appear to be moderate, while the macrocracks affect considerably the mechanical response. In addition, the simulations show that the main cracks are first caused by temperature gradients, and then propagate due to a combined action of temperature and capillary pressure gradients.

Acknowledgements

This work was performed within the framework of DSNI/Reactors project at CEA. Financial support from EDF is gratefully acknowledged.

Appendix A

Composition of the concrete:

Composition	kg/m^3
Sand 0/5	788
Aggregate 5/12.5	309
Aggregate 12,5/25	767
Ciment CEM II 55 PM	340
Plasticizer: plastiment HP	1.22
Water	210

In the sequel are listed the expressions retained for parameters and functions used in the numerical simulations.

Gas permeability coefficient k_{mg} [28]:

$$k_{mg} = k^*_{mg} k_{rg}\left(1 + \frac{a}{p_g}\right) \quad \text{in } m^2 \quad \text{with } k^*_{mg} = k_{mg}(S_l = 0) \tag{A.1}$$

where p_g is the gas pressure and a a coefficient. The relative permeability to gas k_{rg} reads [27]:

$$k_{rg}(S_l) = (1 - S_l)^p (1 - S_l^{1/m})^{2\,m} \tag{A.2}$$

in which the coefficients identified on a CEM I concrete with w/c = 0.48 are: $a = 11.1$, $p = 5.5$ and $m = 0.56$ [28]. Expression for the relative permeability to water k_{rl} [27]:

$$k_{rl}(S_l) = \sqrt{S_l}(1 - (1 - S_l^{1/m})^m)^2 \quad \text{with } m = 0.5 \tag{A.3}$$

Expression of the water density, saturation vapor pressure and heat of vaporization [33]:

$$\rho_l = 314.4 + 685.6\left[1 - \left(\frac{T - 273.15}{374.14}\right)^{\frac{1}{0.55}}\right]^{0.55} \text{ in kg/m}^3 \tag{A.4}$$

$$p_{vs}(T) = p_{atm}\exp\left[4871.3\frac{T - 100}{373.15(T + 273.15)}\right] \text{ in Pa} \tag{A.5}$$

$$L_{l\to v} = \frac{2450.25 - 6.434T}{1 - 0.0019,057T - 7.0024\times 10^{-7}T^2} \text{ in kJ/kg} \tag{A.6}$$

Expression of gas–liquid interfacial tension [34]:

$$\sigma_{gl} = 0.1558\left(1 - \frac{T}{647.1}\right)^{1.26} \text{ in N/m} \tag{A.7}$$

Expression of the dynamic viscosities [35]:

$$\eta_l(T) = 2.414\times 10^{-5}\exp\left(\frac{570.58058}{T + 133.15}\right) \text{ in kg/m/s}$$

$$\eta_v(T) = 3.85\times 10^{-8}T + 10^{-5} \tag{A.8}$$

Expression of the thickness of the adsorbed water layer [36]:

$$t = 3.85 - 1.89(\ln(-\ln(h_r)) \text{ in Å} \tag{A.9}$$

Expression of the heat capacity of dry solid phase:

Quantity of bound water	$0.9 \times 0.21 \times$ mass of cement
Heat of dehydration $L_{s\to l}$	2500 kJ/kg
Heat capacity of anhydrous cement C_c	760 J/(kg °C)
Heat capacity of aggregate C_g	840 J/(kg °C)
Heat capacity of free water C_{pl}	4184 J/(kg °C)
Heat capacity of bound water C_{bw}	3760 J/(kg °C)
Heat capacity of dry solid phase C_{ds}	$(C_c\, m_c + C_g m_g)/(m_c + m_g)$

References

[1] R. Lewis, B.A. Schrefler, The finite element method in the static and dynamic deformation and consolidation of porous media, John Wiley & Sons, New York, 1998.

[2] O. Coussy, Poromechanics, John Wiley & Sons, New York, 2004.

[3] D. Gawin, C.E. Majorana, B.A. Schrefler, Numerical analysis of hygro-thermal behaviour and damage of concrete at high temperature, Mech. Cohesive-Friction. Mater. 4 (1) (1999) 37–74.

[4] N. Khalili, B. Loret, An elasto-plastic model for non-isothermal analysis of flow and deformation in unsaturated porous media: Formulation, Int. J. Solids Struct. 38 (46–47) (2001) 8305–8330.

[5] J. Rutqvist, L. Börgesson, M. Chijimatsu, A. Kobayashi, L. Jing, T.S. Nguyen, J. Noorishad, C.F. Tsang, Thermohydromechanics of partially saturated geological media: Governing equations and formulation of four finite element models, Int J. Rock Mech. Mining Sci. 38 (1) (2001) 105–127.

[6] S. Grasberger, G. Meschke, Thermo-hygro-mechanical degradation of concrete: From coupled 3D material modelling to durability-oriented multifield structural analyses, Mater. Struct./Mater. Construct. 37 (268) (2004) 244–256.

[7] B. Bary, J.P. Bournazel, E. Bourdarot, Poro-damage approach applied to hydro-fracture analysis of concrete, J. Eng. Mech. 126 (9) (2000) 937–943.

[8] J.F. Shao, H. Zhou, K.T. Chau, Coupling between anisotropic damage and permeability variation in brittle rocks, Int. J. Numer. Anal. Methods Geomech. 29 (12) (2005) 1231–1247.

[9] W.G. Gray, B.A. Schrefler, Thermodynamic approach to effective stress in partially saturated porous media, Europ. J. Mech. – A/Solids 20 (4) (2001) 521–538.

[10] V. Baroghel-Bouny, M. Mainguy, T. Lassabatere, O. Coussy, Characterization and identification of equilibrium and transfer moisture properties for ordinary and high-performance cementitious materials, Cement Concrete Res. 29 (8) (1999) 1225–1238.

[11] B. Bary, A polydispersed particle system representation of the porosity for non-saturated cementitious materials, Cement Concrete Res. 36 (11) (2006) 2061–2073.

[12] B. Bary, Estimation of mechanical and transfer parameters in unsaturated microcracked concrete, submitted for publication.

[13] S. Dal Pont, A. Ehrlacher, Numerical and experimental analysis of chemical dehydration, heat and mass transfers in a concrete hollow cylinder submitted to high temperatures, Int. J. Heat Mass Transfer 47 (1) (2004) 135–147.

[14] H. Horii, S. Nemat-Nasser, Overall moduli of solids with microcracks: load-induced anisotropy, J. Mech. Phys. Solids 31 (2) (1983) 155–171.

[15] J. Aboudi, Y. Benveniste, Effective moduli of cracked bodies in plane deformations, Eng. Fract. Mech. (231) (1986) 171–184.

[16] L. Dormieux, D. Kondo, Micromechanical approach to the coupling between permeability and damage [Approche micromécanique du couplage perméabilité-endommagement], CR – Mec. 332 (2) (2004) 135–140.

[17] L. Dormieux, D. Kondo, F.J. Ulm, Microporomechanics, John Wiley & Sons, Chichester, 2006.

[18] Q.S. Zheng, D.X. Du, An explicit and universally applicable estimate for the effective properties of multiphase composites which accounts for inclusion distribution, J. Mech. Phys. Solids 49 (11) (2001) 2765–2788.

[19] S. Torquato, Random Heterogeneous Media: Microstructure and Macroscopic Properties, Springer-Verlag, New York, 2001.

[20] G.J. Dvorak, Transformation field analysis of inelastic composite materials, Proc. Roy. Soc. A 437 (1992) 311–327.

[21] D. Gawin, F. Pesavento, B.A. Schrefler, Hygro-thermo-chemo-mechanical modelling of concrete at early ages and beyond. Part II: Shrinkage and creep of concrete, Int. J. Numer. Methods Eng. 67 (3) (2006) 332–363.

[22] M. Mainguy, O. Coussy, V. Boroghel-Bouny, Role of air pressure in drying of weakly permeable materials, J. Eng. Mech. 127 (6) (2001) 582–592.

[23] H. Loosveldt, Z. Lafhaj, F. Skoczylas, Experimental study of gas and liquid permeability of a mortar, Cement Concrete Res. 32 (9) (2002) 1357–1363.

[24] V. Baroghel-Bouny, Caractérisation des pâtes de ciment et des bétons. Méthodes, analyse et interprétations, PhD thesis (in french), LCPC, 1994.

[25] D.S. McLachlan, An equation for the conductivity of binary mixtures with anisotropic grain structures, J. Phys. C: Solid State Phys. 20 (1987) 865–877.

[26] J.G. Berryman, Bounds and estimates for transport coefficients of random and porous media with high contrasts, J. Appl. Phys. 97 (6) (2005) 1–11.

[27] M.T. van Genuchten, Closed-form equation for predicting the hydraulic conductivity of unsaturated soils, Soil Sci. Soc. Am. J. 44 (5) (1980) 892–898.

[28] J.P. Monlouis-Bonnaire, J. Verdier, B. Perrin, Prediction of the relative permeability to gas flow of cement-based materials, Cement Concrete Res. 34 (5) (2004) 737–744.
[29] P.I. Ravikovitch, A.V. Neimark, Experimental confirmation of different mechanisms of evaporation from ink-bottle type pores: equilibrium, pore blocking, and cavitation, Langmuir 18 (25) (2002) 9830–9837.
[30] R. Černý, P. Rovnaníková, Transport Processes in Concrete, Spon Press, 2002.
[31] Z.P. Bazant, M. Kaplan, Concrete at High Temperatures. Material Properties and Mathematical Models, C. d. C. Series, Longman Group Limited, Harlow, 1996.
[32] F.J. Ulm, O. Coussy, Z.P. Bazant, The chunnel fire. I: chemoplastic softening in rapidly heated concrete, J. Eng. Mech. 125 (3) (1999) 272–282.
[33] K. Ranznjevic, Tables et diagrammes thermodynamiques, Eyrolles, 1970.
[34] B. Le Neindre, Tensions superficielles des composés inorganiques et des mélanges. Constantes Mécaniques, Techniques de l'Ingénieur, K476, 1993.
[35] P. Pezzani, Propriétés thermodynamiques de l'eau, K7, no. K585, 1988.
[36] D. Quenard, H. Sallee, Water vapor adsorption and transfer in cement-based materials: a network simulation, Mater. Struct./Mater. Construct. 25 (1992) 515–522.